Additive Manufacturing 60 (2022) 103240

Contents lists available at ScienceDirect

Additive Manufacturing

journal homepage: www.elsevier.com/locate/addma

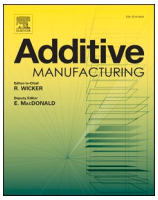

Rapid calculation of part scale residual stress – Powder bed fusion of stainless steel, and aluminum, titanium, nickel alloys

Kajal Khan [a,b], L. Srinivasa Mohan [b], Amitava De [a,*], Tarasankar DebRoy [c]

[a] Department of Mechanical Engineering, Indian Institute of Technology Bombay, 400076, India
[b] Ansys Software Pvt. Ltd., Pune 411057, India
[c] Department of Materials Science and Engineering, The Pennsylvania State University, PA 16801, USA

ARTICLE INFO

Keywords:
Additive manufacturing
Laser powder bed fusion
Part scale
Residual stress distribution
Analytical modeling
Dimensional analysis

ABSTRACT

A novel analytical model is developed to compute the part scale through-thickness longitudinal residual stress distributions and applied for laser powder bed fusion of four commonly used powder alloys. An important input for the analytical modeling calculations is the peak residual stress for a deposited layer, which is estimated using a unique functional relationship and presented as a function of important process conditions for laser powder bed fusion of different powder alloys. The analytically calculated results of longitudinal residual stress distributions through the part and baseplate thickness are tested rigorously with the corresponding numerically computed and experimentally measured results in the literature for laser powder bed fusion of small and large parts involving the deposition of several thousands of layers. It is shown further that the analytical model can serve as a fast and practical design tool to estimate the through-thickness longitudinal residual stress distribution, which is along the length of the part, for part scale laser powder bed fusion using inexpensive computational resources and with appreciable accuracy.

1. Introduction

In laser powder bed fusion (LPBF) of powder alloys, thin layers of powders are melted layer-by-layer under a focused laser beam in a progressive manner that on solidification generates a solid part [1]. The repeated heating and cooling of the layers results in residual stress in the finished part [2]. The residual stress is undesirable and significantly affects the ability of a part to meet the functional requirements, especially under cyclic loading. Therefore, the development of an effective method for the prior estimation of the residual stress distribution is needed to ensure serviceability and avoid premature failure of parts [3]. Computer-based sequentially coupled heat transfer and thermo-mechanical analyses are traditionally undertaken to calculate residual stress distributions for LPBF of parts. However, the macro-scale numerical models require huge computational effort to simulate the building of a realistic part due to a large number of layers [4]. For example, a typical part consists of a scan area of 1000–10000 mm^2 per layer and many thousands of 20–60 μm thick layers, which pose a significant challenge for numerical modeling [5,6]. A layer-by-layer simulation of a build volume as small as $6 \times 2 \times 1.5$ mm^3 requires an approximate CPU time of 2891 days with a uniform discretization of the domain [7]. A remedy is to develop an analytical model for a quick estimation of the residual stress distributions in a part that would help in optimizing the build parameters.

Several researchers used computer-based numerical models for the estimation of residual stress in LPBF. Fu and Guo [8] simulated LPBF of Ti6Al4V for a five-layer build of dimensions $2 \times 0.2 \times 0.15$ mm^3 using the finite element method. The model took nearly 240 h to compute the residual stress distributions through the layers in a personal computer. Tangestani et al. [9] reported a simulation time of around 39,688 CPU hours to analyze the LPBF of a thirty-layer build of dimensions $5 \times 0.5 \times 1.2$ mm^3 with a Nickel-based superalloy powder. The authors could reduce the simulation time to around 264 CPU hours by using a simplified line heat source expression to account for the heat input from the laser beam. Ganeriwala et al. [10] simulated the LPBF of a Ti6Al4V bridge specimen of dimensions $21 \times 9 \times 5$ mm^3 using a lumped layer approach with more than fifteen powder layers lumped into one equivalent computational layer to reduce the simulation run time. For two different equivalent computational layer heights of 0.25 mm and 0.50 mm, the authors reported simulation times of around 7315 and 168 CPU hours, respectively. Hajializadeh and Ince [11] analyzed the LPBF of an eighteen-layer L-shaped specimen of dimension $12 \times 12 \times 1$ mm^3 using a fine mesh and an adaptive mesh, and reported simulation times

* Corresponding author.
E-mail address: amit@iitb.ac.in (A. De).

https://doi.org/10.1016/j.addma.2022.103240
Received 19 June 2022; Received in revised form 16 October 2022; Accepted 16 October 2022
Available online 18 October 2022

Nomenclature

d	Track length.
d_L	Laser spot diameter.
E	Young's modulus.
h	Hatch spacing.
h_b	Baseplate height.
H_m	Enthalpy at melting.
n	Number of layers.
P	Laser power.
Q_b	Heat input per unit build volume.
Q_v	Volumetric heat input.
T_a	Ambient temperature.
T_m	Melting temperature.
T_p	Preheat temperature.
t	Layer thickness.
v	Scanning speed.
w, w_b, w_p	Width, baseplate width, part width.
x, y, z	Directions used for the coordinate system.
Y	Peak residual stress.
α	Thermal diffusivity.
α_0	Reference thermal diffusivity.
β	Coefficient of thermal expansion.
ΔT	Difference between the melting temperature and the preheat temperature.
δ	Melt pool depth.
σ_{x1}	Longitudinal residual stress.
σ_{xnb}, σ_{xnt}, σ_{xnpj}	Longitudinal residual stresses in the baseplate, transition zone and j^{th} layer respectively after the deposition of the n^{th} layer.
σ_y	Yield stress.

of 58 CPU hours and 22 CPU hours, respectively. The impractical huge computation times of these numerical models demand an analytical model that can quickly compute the residual stress distributions through a part-scale build with fair accuracy.

In contrast to the numerical models, the analytical models to compute the thermomechanical residual stress considered the equilibrium of force and moment in an integral form with inherent assumptions of the build as homogeneous, isotropic, and elastic material [12–15]. These models presumed the imposition of tensile stress, equivalent to the material yield stress, due to the thermal shrinkage of a deposited layer and a linear variation of strain through the part and the baseplate. Marcelis and Kruth [13], Boruah et al. [14], and Chahal and Taylor [15] used such analytical models to calculate the residual stress in a block consisting of up to 300 layers. Mirkoohi et al. [16] and Ning et al. [17–19] proposed a plane strain-based stress equilibrium model with the consideration of the local temperature gradient to calculate the thermal stress during the solidification of a layer. The limitation of most of these models is that these models assumed the maximum residual stress during the deposition of a new layer as constant and equal to the material yield stress without considering any effect of the process conditions. In addition to that, these models are validated only for simple parts of rectangular cuboid and the effect of remelting on the residual stress has been neglected.

A novel analytical model is therefore developed in the present work to compute the part scale residual stress distributions and applied for laser powder bed fusion of commonly used alloys namely Ti6Al4V, IN718, IN625, SS316 and AlSi10Mg alloys. The analytical calculations of the residual stress distributions require the values of peak tensile residual stress for a deposited layer and its melt pool depth, which are estimated using scaling analyses. The peak tensile residual stress for deposition of a layer are presented in the form of easy-to-use process maps for LPBF of different alloys. The computational efficiency of the analytical model is highlighted for the estimation of residual stress distribution in part scale in comparison to that using typical numerical models.

2. Analytical modeling of residual stress distribution

During the deposition of the first layer, the upper region of the baseplate experiences a high temperature gradient and thermal expansion. The lower part of the baseplate is colder and more rigid, and cannot expand as much. As a result, the upper layer experiences compressive stress in the top region and balancing tensile stress in the bottom region of the baseplate [13,20]. The experience of the hot upper region is somewhat equivalent to the heating of a solid bar with constraints at each end developing compressive stress. As the molten layer solidifies and undergoes volume shrinkage, the shrinkage is resisted by the baseplate. This results in tensile stress in the deposited layer and balancing compressive stress in the baseplate. Further cooling down of the layer-baseplate assembly to room temperature increases the tensile stress in the deposited layer. Consequently, the compressive stress through the baseplate will increase further with cooling resulting in a little or no tensile stress remaining at the bottom of the baseplate depending on the constraints on the baseplate. Fig. 1 schematically shows the likely distribution of residual stress through the deposit-baseplate thickness after the deposition process.

An analytical model is developed to compute the aforementioned nature of the evolution of residual stress in the printed layers and baseplate based on mechanistic relations. The following simplifying assumptions are made to keep the analytical model tractable.

(a) The material is considered isotropic, homogeneous, and linearly elastic. The material properties are considered to be temperature independent.
(b) The longitudinal component of residual stress is assumed to be dominant based on previous studies [21] and constant along the width direction.
(c) The residual stress is calculated at the mid-length of the part-baseplate assembly, which is considered symmetric about y-z plane at the mid-length.

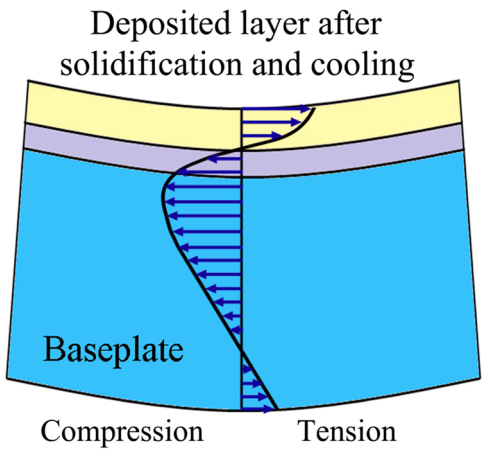

Fig. 1. Schematic presentation of residual stress distribution after solidification and cooling of the layer-baseplate assembly. A transition zone between the layer and baseplate is shown to indicate the transition of the nature of stress.

(d) The longitudinal residual stress is assumed to be independent of the edge effect and scanning strategy. No external forces are considered.
(e) The effect of individual tracks is neglected, and the melting of each layer is considered instantaneous with a complete bonding along the part-baseplate and interfaces between layers. The laser power is considered as the nominal heat input.
(f) The proposed analytical model considers a static equilibrium of force and moment in part and baseplate.
(g) The build part is assumed to have no variation in dimension in the width direction.

Fig. 2 schematically shows an LPBF printed part on a baseplate, the corresponding dimensional nomenclature, and the location for the calculation of longitudinal residual stress. The residual stress evolves due to an equilibrium of force and moment at any cross-section of the part-baseplate assembly and are expressed mathematically as [22].

$$\int \sigma_{x1}(z)wdz = 0 \tag{1}$$

$$\int \sigma_{x1}(z)wzdz = 0 \tag{2}$$

where σ_{x1} is the longitudinal component of residual stress in the x-direction after deposition of layer 1, w denotes the width of the deposited layer or baseplate, and wdz refers to an elemental area on which σ_{x1} is working.

As the longitudinal residual stress in the part-baseplate assembly is continuous, the integrals in Eqs. (1 and 2) can be decomposed and assessed separately for the baseplate and deposited layers. The through-thickness variation of longitudinal residual stress in individual layers is not prominent due to the small thickness of the layers, which are generally 20–100 μm thick [23], and is assumed to be constant [23,24]. This constant longitudinal residual stress is considered to be equilibrated by a linearly varying compressive to tensile stress through the baseplate. There is a transition of stress at the interface of the baseplate and deposited layer as shown in Fig. 1. The stresses in a deposited layer, baseplate, and transition zone which goes into the integrals in Eqs. (1 and 2) can therefore be given as

$$\sigma_{x1p1}(z) = Y \tag{3}$$

$$\sigma_{x1b}(z) = E_b(a_1 z + b_1) \tag{4}$$

$$\sigma_{x1t}(z) = E_b[c_1\{z - (h_b - \delta)\} + d_1] \tag{5}$$

where $\sigma_{x1p1}(z)$, $\sigma_{x1b}(z)$ and $\sigma_{x1t}(z)$ are stresses in the x-direction at any height z measured from the bottom of the baseplate in layer 1, the baseplate, and the transition zone, respectively, Y is the peak tensile residual stress in layer 1, E_b is Young's modulus of baseplate material, δ is the thickness of the transition zone and considered as equal to the melt pool depth, h_b is the baseplate height, and, a_1, b_1, c_1 and d_1 are constants.

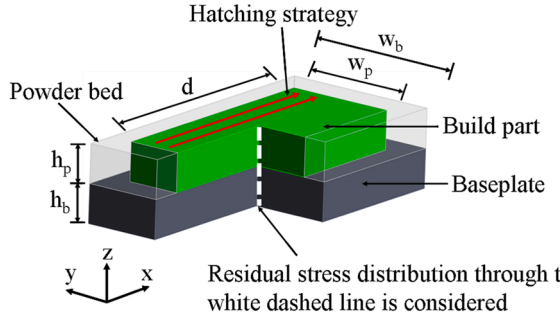

Fig. 2. Schematic presentation of an LPBF printed part on a baseplate, the corresponding dimensional nomenclature and the location for the calculation of through-thickness longitudinal residual stress distribution.

As more layers are deposited, the stress will accumulate in the solidified layers and the baseplate. The incremental stress in the solidified layers and baseplate due to every newly deposited layer is assumed as a linear function of z with slope and intercepts as a_i and b_i respectively where "i" indicates the current layer number. This incremental stress is calculated recursively for the deposition of each new layer. Every layer in the part undergoes different stress as they are subjected to different stress increment based on its sequence of deposition. This leads to a nonlinear distribution of stress in the part as a whole. Considering a linear superposition of stress, the distribution of residual stress through the baseplate and deposited layers for the deposition of n number of layers can be expressed as

$$\sigma_{xnb}(z) = E_b \sum_{i=1}^{n}(a_i z + b_i) \tag{6}$$

$$\sigma_{xnpj}(z) = Y + E_{pj} \sum (a_i z + b_i) H\{(i-j)t - \delta\} \text{ for } (j+1) \le i \le n \tag{7}$$

where $\sigma_{xnb}(z)$ is the residual stress in the baseplate, $\sigma_{xnpj}(z)$ is the residual stress in any layer j after the deposition of the n^{th} layer ($j < n$), E_{pj} is the Young's modulus of the j^{th} layer of powder alloy, t is the layer thickness and, a_i and b_i are constants. The term $H\{(i-j)t-\delta\}$ in Eq. (7) is a Heaviside function, which is equal to zero for $\{(i-j)t-\delta\} < 0$ and, unity for $\{(i-j)t-\delta\} \ge 0$. The summation term in the right-hand side of Eq. (7) accounts for either the nullification of residual stress in a layer due to its remelting or the redistribution of residual stress in a layer in case there is no remelting during the deposition of successive upper layers.

The residual stress $\sigma_{xnpn}(z)$ in the n^{th} layer and $\sigma_{xnt}(z)$ in the transition zone are written similarly following Eqs. (3) and (5) as

$$\sigma_{xnpn}(z) = Y \tag{8}$$

$$\sigma_{xnt}(z) = E_b[c_n\{z - (h_b - \delta)\} + d_n] \tag{9}$$

where c_n and d_n are constants and are given in terms of a_n and b_n as

$$c_n = \frac{1}{\delta}\left[\frac{Y}{E_b} - d_n + \frac{E_{p1}}{E_b}\sum_{i=2}^{n}(a_i h_b + b_i)H\{(i-1)t - \delta\}\right] \tag{10}$$

$$d_n = \sum_{i=1}^{n}\{a_i(h_b - \delta) + b_i\} \tag{11}$$

Therefore Eqs. (1 and 2) can be written in a generalized form for the deposition of n layers as

$$\int_0^{(h_b-\delta)} \sigma_{xnb} w_b dz + \int_{(h_b-\delta)}^{h_b} \sigma_{xnt} w_b dz + \int_{h_b}^{(h_b+t)} \sigma_{xnp1} w_p dz + \ldots\ldots + \int_{(h_b+mt)}^{(h_b+nt)} Y w_p dz = 0 \tag{12}$$

$$\int_0^{(h_b-\delta)} \sigma_{xnb} w_b z dz + \int_{(h_b-\delta)}^{h_b} \sigma_{xnt} w_b z dz + \int_{h_b}^{(h_b+t)} \sigma_{xnp1} w_p z dz + \ldots\ldots + \int_{(h_b+mt)}^{(h_b+nt)} Y w_p z dz = 0 \tag{13}$$

where m = (n-1), w_b is the baseplate width, and w_p is the layer width. Eqs. (6–11) are used to evaluate the integrals in Eqs. (12 and 13) and can be expressed in corresponding algebraic forms as

$$a_n e_n + b_n f_n = g_n \tag{14}$$

$$a_n q_n + b_n r_n = s_n \quad (15)$$

where e_n, f_n, g_n, q_n, r_n, s_n are constants. For every new layer deposited, the terms a_n and b_n are solved recursively using Eqs. (14 and 15). These an and bn are used to compute the overall distribution of residual stress through the printed layers and the baseplate using Eqs. (6–11). A prior estimation of the melt pool depth (δ) and the peak tensile residual stress (Y) for deposition of a new layer is required for recursive simulations of Eqs. (14 and 15), which are developed through novel scaling analyses and presented in the following sections. The proposed analytical model considers the evolution of only the longitudinal component residual stress to keep the overall calculations tractable. A further extension of the proposed analytical model to compute the layer-by-layer evolution of the three-dimensional residual stress field will be addressed in the future.

2.1. Estimation of melt pool depth (δ)

A scaling analysis is carried out using the Buckingham π-theorem to estimate the melt pool depth (δ) for the deposition of a layer as function of important LPBF conditions. Table 1 shows the variables and their units and dimensions in the MLT system that are considered for the dimensional analysis where M, L and T stand for mass, length, and time, respectively. The volumetric heat input Q_v is computed as $P/(vd_Lt)$ [25,26], where P, v, d_L, and t are laser power, scanning speed, spot diameter, and layer thickness, respectively, and assumed in a dimensionless form as Q_v/H_m, where H_m is the enthalpy at melting for a powder alloy. The preheat temperature T_p is considered as T_p/T_a where T_a is the ambient temperature. The thermal diffusivity (α) is introduced to account for the intrinsic thermal behavior of individual powder alloys and considered in a non-dimensional form as α/α_0, where α_0 is a reference thermal diffusivity which is considered same as the diffusivity of Ti6Al4V. Tables 2 and 3 show the alloy properties [27–29] and the ranges of LPBF conditions [25,30–49], which are used for the dimensional analysis.

Table 1 shows one fundamental dimension L and a total of five variables. Four (5 – 1 = 4) π terms (π_1, π_2, π_3, π_4) are therefore formed following Buckingham π-theorem as

$$\pi_1 = \frac{\delta}{t}; \quad (16)$$

$$\pi_2 = \frac{Q_v}{H_m}; \quad (17)$$

$$\pi_3 = \frac{T_p}{T_a}; \quad (18)$$

$$\pi_4 = \frac{\alpha}{\alpha_0} \quad (19)$$

The term π_1 depicts dimensionless melt pool depth (δ/t) and is directly proportional to both π_2 and π_3, which refer to the dimensionless heat input (Q_v/H_m) and preheat temperature (T_p/T_a) of the baseplate and the solidified layers, respectively [25,26,34,35,50]. In contrast, dimensionless melt pool depth (δ/t) is inversely affected by (α/α_0) as a high rate of heat diffusion decreases the peak temperature and melt pool dimensions [51]. A functional relation of π_1 in terms of π_2, π_3, and π_4 is therefore comprehended as

Table 1
Parameters used for dimensional analysis of melt pool depth (δ).

Parameters	Symbol	Unit	Dimension
Dimensionless heat input	Q_v/H_m	–	–
Dimensionless preheat temperature	T_p/T_a	–	–
Dimensionless thermal diffusivity	α/α_0	–	–
Melt pool depth	δ	m	L
Layer thickness	t	m	L

Table 2
Physical properties of alloys used for non-dimensional analysis [27–29].

	β ($\times 10^{-6}$) K^{-1}	α ($\times 10^{-6}$) m^2/s	T_m (K)	σ_y (MPa)	E (GPa)	H_m ($\times 10^6$) (J/m^3)
Ti6Al4V	10.1	1.626	1933	1050	110	6494
IN718	13.1	3.082	1533	634	207	8014
IN625	12.8	2.693	1623	720	205	8868
SS316	18.6	5.409	1648	500	206	9540
AlSi10Mg	23.0	43.948	868	275	68	2776

Table 3
Range of various parameters considered from literature [25,30–49].

	Ti6Al4V	IN718, IN625	SS316	AlSi10Mg
P (W)	70–520	40–370	90–800	150–400
v (m/s)	0.2–2.0	0.2–2.5	0.1–1.8	0.2–2.4
h (μm)	60–110	80–120	56–150	100–170
t (μm)	30–40	20–40	25–50	30–90
d_L (μm)	95–140	75–100	54–262	70–150
d (mm)	5	5	2.5–10	6.5–10
Y (MPa)	313–634	193–501	99–448	51–140
δ (μm)	35–400	8–458	30–479	46–232
T_p (°C)	25–400	25–500	25	25–160

$$\pi_1 = g(\pi_2, \pi_3, 1/\pi_4) \quad (20)$$

The final form of Eq. (20) is obtained as Eq. (21) by plotting all the experimentally measured (δ/t) values from the literature [25,30–40] for LPBF of five powder alloys as a function of the corresponding dimensionless variables (Q_v/H_m), (T_p/T_a) and (α/α_0) in Fig. 3.

$$\frac{\delta}{t} = 0.4255\left(\frac{Q_v}{H_m}\frac{T_p}{T_a}\frac{1}{\sqrt{\alpha/\alpha_0}}\right)^{0.8863} \quad (21)$$

Eq. (21) confirms to a power-law relation with the corresponding correlation coefficient (R^2) as 0.87. Fig. 3 includes around 260 data points and together, they show a generalized intuitive trend for LPBF of five commonly used powder alloys. The computed melt pool depth from Eq. (21) for an LPBF condition is finally used for the recursive

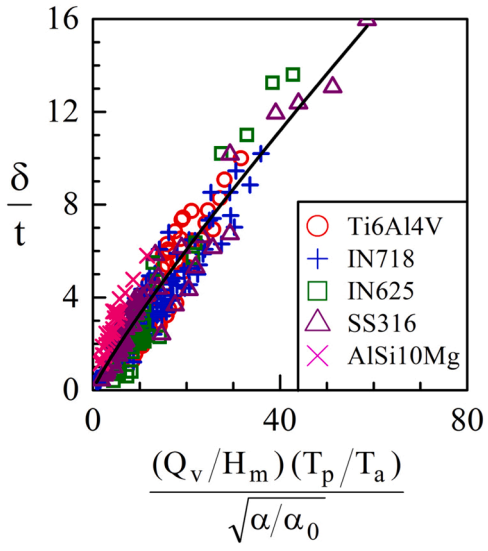

Fig. 3. Variation of dimensionless melt pool depth as a function of three dimensionless variables for LPBF of five different powder alloys. The best fit line (in black) is obtained by using the least square method. The experimentally measured melt pool depths for LPBF of these powder alloys are obtained from literature: Ti6Al4V [30,31], IN718 [32–35], IN625 [36,37], SS316 [25,38], AlSi10Mg [39,40].

calculations of residual stress distributions through the printed layers and baseplate following Eqs. (14 and 15).

2.2. Estimation of peak residual stress (Y)

A similar scaling analysis is carried out using the Buckingham π-theorem to estimate the peak residual stress (Y) for the deposition of a layer as a function of important LPBF conditions. Table 4 shows the list of variables, and their units and dimensions in the MLT system, which are considered for scaling analysis of peak residual stress for the deposition of a layer using the Buckingham π-theorem. The term Q_b is the heat input per unit build volume and computed as P/(vht) [39,40,43,46], where P, v, t, and h are laser power, scanning speed, layer thickness, and hatch spacing, respectively. Further, Q_b is assumed in a dimensionless form as Q_b/H_m, where H_m is the enthalpy at melting for a powder alloy. The variable $\beta\Delta T$ refers to thermal strain where β is the coefficient of thermal expansion or contraction and ΔT is the difference between the melting and the preheat temperatures. The other variables in Table 4 include the dimensionless preheat temperature (T_p/T_a) and thermal diffusivity (α/α_0), laser spot diameter (d_L), and the deposited track length (d) for a layer. The peak tensile residual stress (Y) is considered as a dimensionless ratio (Y/σ_y), where σ_y is the yield strength of the powder alloy material.

Table 4 shows one fundamental dimension L and a total of seven variables. Six (7 – 1 = 6) π terms (π_1, π_2, π_3, π_4, π_5, and π_6) are therefore formed following Buckingham π-theorem as

$$\pi_1 = \frac{Y}{\sigma_y}; \tag{22}$$

$$\pi_2 = \frac{Q_b}{H_m}; \tag{23}$$

$$\pi_3 = \beta\Delta T; \tag{24}$$

$$\pi_4 = \frac{T_p}{T_a}; \tag{25}$$

$$\pi_5 = \frac{d}{d_L}; \tag{26}$$

$$\pi_6 = \frac{\alpha}{\alpha_0} \tag{27}$$

The dimensionless peak residual stress term π_1 i.e., (Y/σ_y) is influenced directly by π_2, π_3, and π_5, and inversely by π_4 and π_6. This is intuitive as an increase in the dimensionless heat input term π_2 results in a larger melt pool and higher residual stress [45,52]. Likewise, an increase in the thermal strain ($\beta\Delta T$) i.e. π_3 results in greater residual stress [53]. A longer track (d) leads to more heat accumulation and temperature gradient (ΔT) thereby increasing residual stress [20,21]. In contrast, the temperature gradient (ΔT) is reduced for a higher preheat temperature resulting in lower residual stress and thus, π_4 affects the dimensionless peak residual stress term π_1 i.e., (Y/σ_y) inversely. Likewise, an increase in the dimensionless thermal diffusivity (α/α_0) implies a greater rate of heat diffusion and lesser heat accumulation resulting in a reduced temperature gradient and a decrease in residual stress [54,55]. A functional relation of π_1 in terms of π_2, π_3, π_4, π_5, and π_6 is therefore presumed as

$$\pi_1 = f(\pi_2, \pi_3, 1/\pi_4, \pi_5, 1/\pi_6) \tag{28}$$

Fig. 4(a) shows around eighty experimentally measured (Y/σ_y) values from the literature [32,41–49] for LPBF of five powder alloys as a function of the corresponding dimensionless variables (Q_v/H_m), ($\beta\Delta T$), (T_p/T_a) and (d/d_L) and (α/α_0). The data points in Fig. 4(a) indicate a power-law relation. A unified relation of (Y/σ_y) is therefore obtained as

$$\frac{Y}{\sigma_y} = 0.5124\left[\frac{(Q_b/H_m)(\beta\Delta T)\sqrt{d/d_L}}{(T_p/T_a)\sqrt{\alpha/\alpha_0}}\right]^{0.6403} \tag{29}$$

with the corresponding correlation coefficient (R^2) as 0.75. The parameter on the right-hand side in Eq. (29) is a product of five dimensionless variables and depicts a factor to scale the residual stress of a layer from the yield stress of the alloy powder for a given LPBF conditions and powder properties. The computed peak residual stress from Eq. (29) for an LPBF condition is finally used for the recursive calculations of residual stress distributions through the printed layers and baseplate following Eqs. (14 and 15). Eq. (29) is also used to generate a set of process maps of peak residual stress for LPBF of different alloys that not only help in analytical calculations of residual stress distributions through the printed part, but also provide a practical route to select LPBF conditions for reducing residual stress. In absence of available experimental results of peak residual stress for part scale LPBF with diverse conditions, FEM-based analyses for LPBF of small deposits may provide data sets for the development of a relation similar to Eq. (29) although the computed results would also be required to be validated through at least a few sets of experiments.

3. Process maps of peak residual stress (Y)

Eq. (29) is used to generate maps of peak residual stress as a function of important LPBF conditions for different powder alloys, which can assist in a careful selection of the process conditions to mitigate residual stress in the final part. These maps can also be used to fetch the value of the peak residual stress as an input for the calculation of residual stress distributions through the part and baseplate following the proposed analytical model. It is further noteworthy that the maps of the peak

Table 4
Parameters used for dimensional analysis of residual stress (Y).

Parameters	Symbol	Unit	Dimension
Dimensionless heat input per unit build volume	Q_b/H_m	–	–
Thermal strain	$\beta\Delta T$	–	–
Dimensionless preheat temperature	T_p/T_a	–	–
Laser spot diameter	d_L	m	L
Track length	d	m	L
Dimensionless thermal diffusivity	α/α_0	–	–
Dimensionless peak residual stress	Y/σ_y	–	–

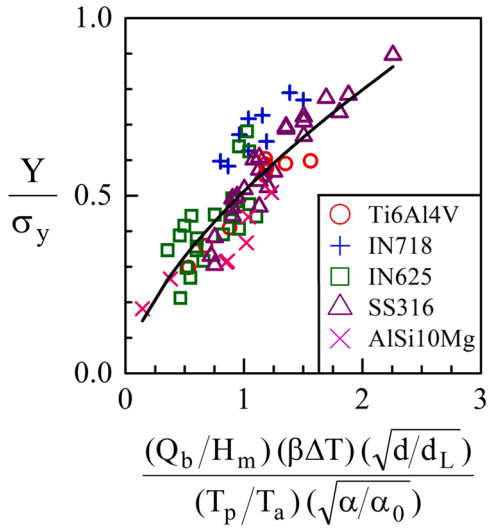

Fig. 4. (a) Variation of measured (Y/σ_y) as a function of five dimensionless variables for LPBF of five different powder alloys. The best fit line (in black) is obtained by using the least square method. The experimentally measured peak residual stress (Y) for LPBF are obtained from literature: Ti6Al4V [41,42], IN718 [32], IN625 [43], SS316 [44–46], AlSi10Mg [47–49].

residual stress for a wide range of combinations are generated following Eq. (29) in a time-efficient manner since it does not require any time-consuming thermomechanical simulations.

Fig. 5 shows the (Y/σ_y) maps for different powder alloys as a function of laser power and scanning speed with the other conditions remaining constant. The (Y/σ_y) map for IN625 is not shown as it shows similar behavior as that of IN718. Fig. 5(a-d) shows an increase in residual stress with laser power, which is attributed to increased heat input. In contrast, the residual stress reduces with an increase in the scanning speed, which is attributed to a decrease in the heat input per unit length. Together these plots show that high laser power and low scanning speed increase residual stress for LPBF of all four alloys. The (Y/σ_y) lines are the steepest for Ti6Al4V due to its lowest thermal diffusivity, which leads to greater heat accumulation and stress. In contrast, the (Y/σ_y) lines are the most gentle for AlSi10Mg, which is attributed to its highest thermal diffusivity among the powder alloys considered here. The residual stress contours for IN718 and SS316 are similar due to their competitive thermophysical properties. The thermal diffusivity of SS316 is around 30 % higher than that of IN718, which leads to a reduced temperature gradient for the SS316 part. In contrast, the coefficient of thermal expansion and contraction (CTE) of SS316 is approximately 40 % higher than that of IN718, which results in a higher thermal strain for a similar temperature gradient for the SS316 part. As a result of these two competitive effects, the (Y/σ_y) maps for SS316 and IN718 show a similar trend.

Fig. 6 shows the maps of (Y/σ_y) as a function of laser power and preheating temperature for four different alloys. The residual stress increases with an increase in the laser power, which is obvious. In contrast, an increase in the preheat temperature reduces the residual stress, which is attributed to reduced thermal strain. Overall, Fig. 6(a-d) show that both high laser power and low preheat temperature result in the accumulation of high residual stress for LPBF of all four alloys. The lines of (Y/σ_y) are the steepest for Ti6Al4V while it is the most gentle for AlSi10Mg. This is attributed to the significantly lower thermal diffusivity of Ti6Al4V as compared to AlSi10Mg, which leads to greater heat accumulation for Ti6Al4V part with increasing laser power. The preheat temperature also affects the slope of (Y/σ_y) lines. For example, a lesser CTE of Ti6Al4V than AlSi10Mg results in smaller thermal strain for LPBF of Ti6Al4V. The residual stress contours for SS316 and IN718 are similar due to their thermo-physical properties as explained earlier.

Fig. 7 shows the maps of (Y/σ_y) for different combinations of laser scanning speed and preheating temperature for LPBF of four different powder alloys with the other process conditions remaining constant. An increase in the scanning speed reduces the residual stress due to a decrease in the heat input per unit length with an increase in the scanning speed. In contrast, as the preheat temperature increases the residual stress decreases due to a decrease in the thermal strain. Overall, Fig. 7(a-d) shows that lower scanning speed and preheat temperature can lead to higher residual stress for LPBF of all four alloys. The steeper slopes of the (Y/σ_y) lines for AlSi10Mg in Fig. 7(d) are attributed to faster diffusion of heat due to the highest thermal diffusivity.

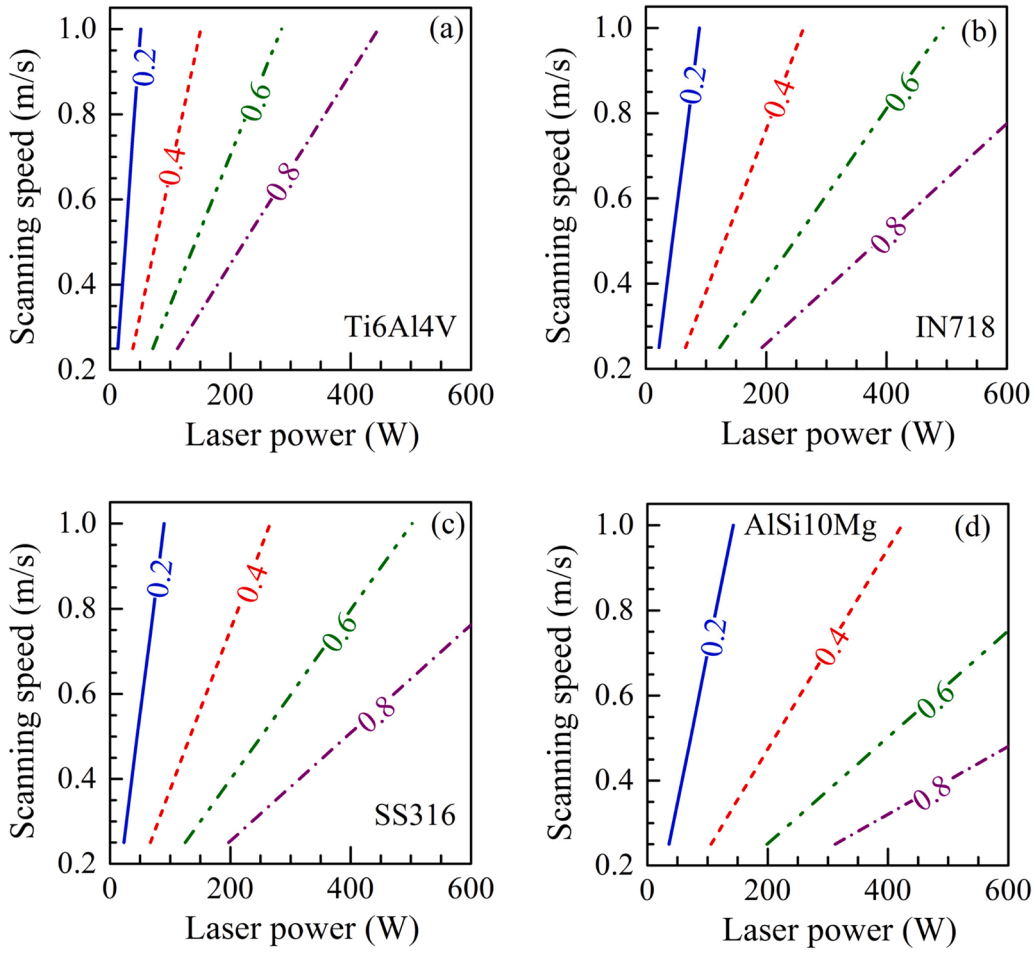

Fig. 5. Process maps showing the variation of (Y/σ_y) for a different combination of laser power and scanning speed for LPBF of (a) Ti6Al4V, (b) IN718, (c) SS316 (d) AlSi10Mg alloy calculated using Eq. (29). Other process parameters are kept constant as: laser spot diameter = 100 μm, layer thickness = 40 μm, hatch spacing = 100 μm, track length = 5 mm, preheat temperature = 298 K.

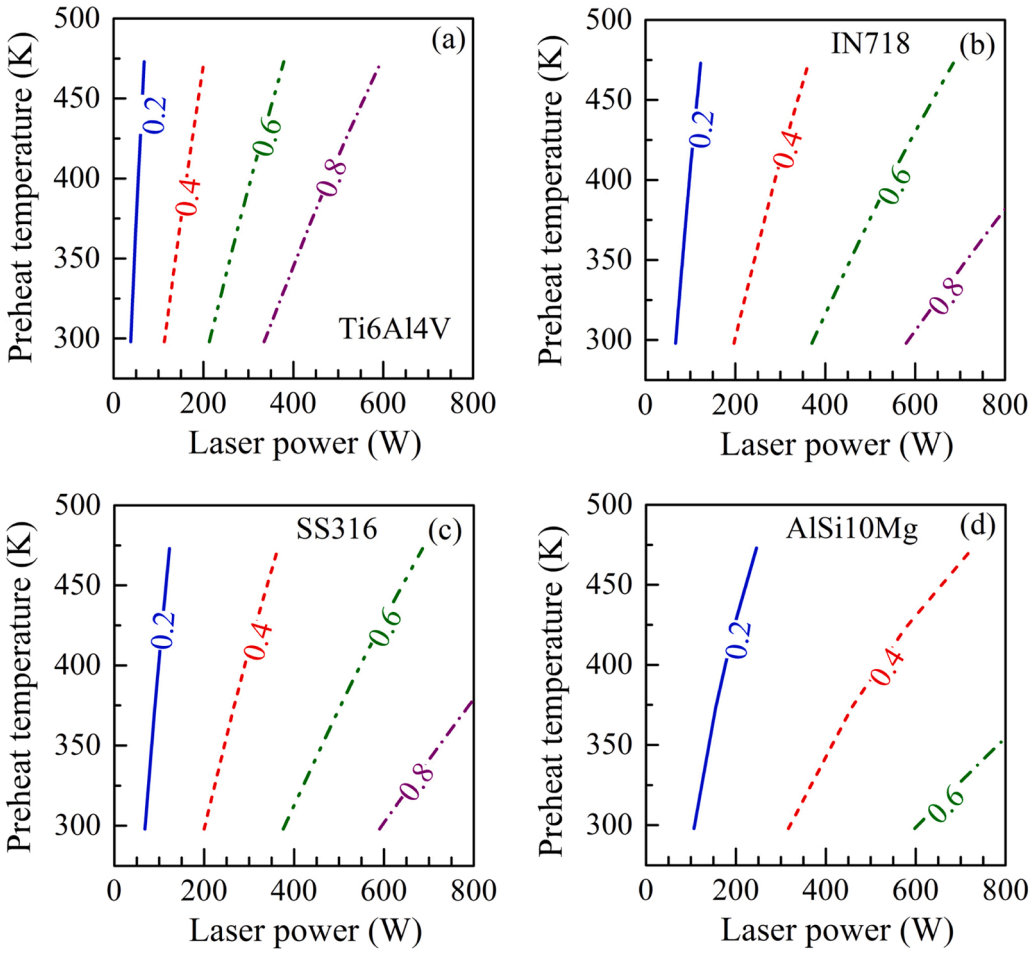

Fig. 6. Process maps showing the variation of (Y/σ_y) for different combinations of laser power and preheat temperature for LPBF of (a) Ti6Al4V, (b) IN718, (c) SS316 (d) AlSi10Mg alloy calculated using Eq. (29). Other process parameters are kept constant as: scanning speed = 750 mm/s, laser spot diameter = 100 μm, layer thickness = 40 μm, hatch spacing = 100 μm, track length = 5 mm.

4. Model testing for multiple alloys

For LPBF of a realistic part, several hundreds and thousands of powder layers are deposited. An attempt is therefore made in the following sections to demonstrate the use of the proposed analytical model for the calculation of residual stress distributions for LPBF of multi-layered wall structures of different powder alloys and a typical real-life part. Four cases where experimentally determined or numerically computed distributions of residual stress have been reported are simulated and the computed results are compared with the corresponding residual stress reported in the literature. These four examples are as follows: (a) a 22 layers deposit of Ti6Al4V, (b) a 334 layers deposit of AlSi10Mg, (c) a 2000 layers deposit of IN718, and (d) a typical realistic demonstrator part of IN625 of 625 layers, all for LPBF.

4.1. LPBF of a 22-layer deposit of Ti6Al4V

The performance of the analytical model to calculate the residual stress distributions for LPBF of a part with 22 layers of Ti6Al4V powder is illustrated in this section using the process conditions from the literature [56]. The authors in reference [56] have used a two-dimensional finite element method-based thermo-mechanical model using the COMSOL multiphysics environment with one-way coupling to compute the residual stress. The heat transfer problem is solved first, and the spatial and temporal distributions of temperature are used as a thermal load to the stress equilibrium problem. For the heat transfer problem, radiation and convection boundary conditions are applied to the top surface of the deposited layer whereas a fixed temperature is applied to the bottom of the baseplate. For the stress analysis, the bottom of the baseplate is fixed in all directions. Fig. 8(a) shows the cross-section of the part and baseplate [56]. The residual stress distribution is analytically computed along the blue dashed line in Fig. 8(a) and compared with the corresponding numerically computed results from the literature [56] in Fig. 8(b). The melt pool depth (δ) and the peak residual stress (Y) are estimated as 70 μm and 913 MPa from Eqs. (21) and (29), respectively, and used as input for the analytical model calculations. The evolution of the residual stress through the layers and the baseplate is computed recursively for the deposition of each new layer following Eqs. (14 and 15).

The numerically computed residual stress distributions [56] in Fig. 8 (b) show a non-linear trend through the part with the peak tensile stress as 1084 MPa at the topmost layer that reduces gradually through the layers to around 1013 MPa at the bottom of the part followed by a sharp transition to a compressive stress of around 79 MPa at the part-baseplate interface. Further, the residual stress shows a nearly linear variation through the baseplate with a compressive stress of around 14 MPa at the bottom of the baseplate. In comparison, the analytically computed results in Fig. 8(b) show a gradual decrease of residual stress from 913 MPa to 714 MPa at the bottom of the part followed by a sharp transition to a compressive stress of around 160 MPa through the part-baseplate interface. Further distribution of stress through the baseplate shows a linear variation and a tensile stress of around 99 MPa at the bottom. Overall, the redistribution of stress remains small due to only a small number of deposited layers.

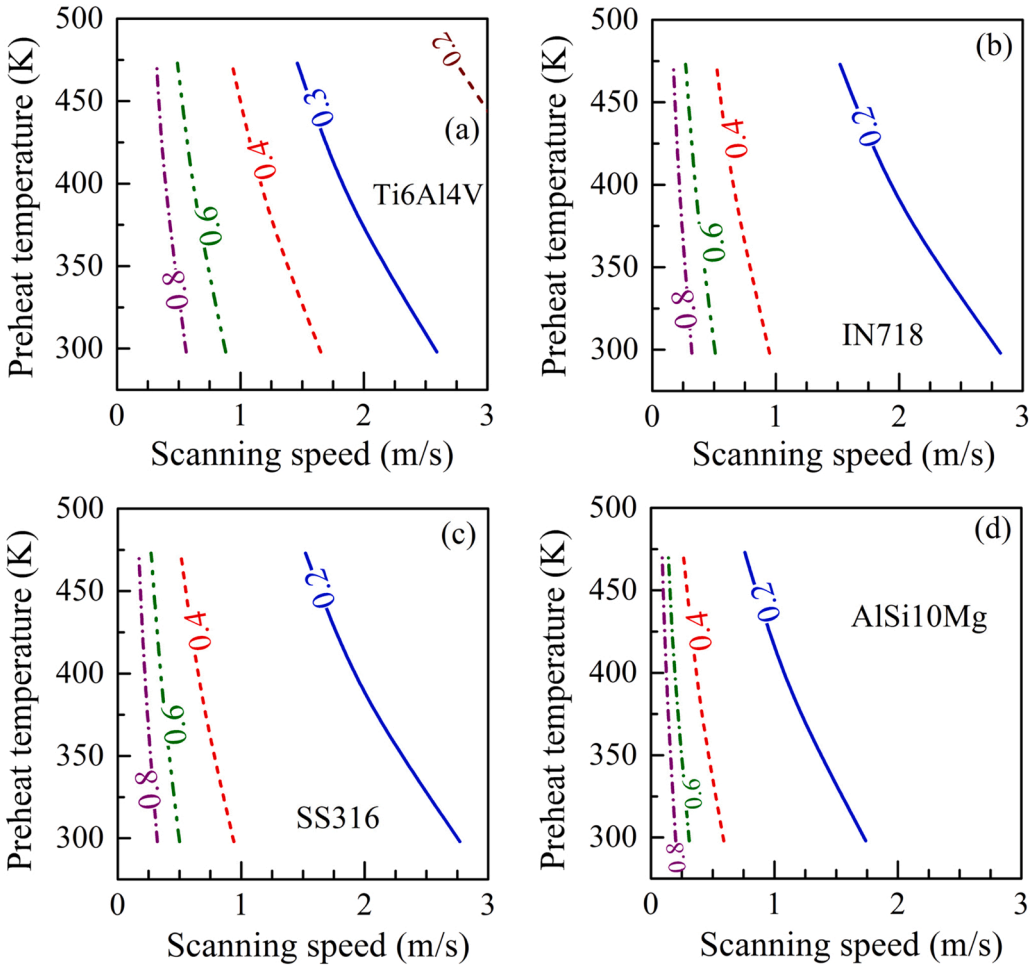

Fig. 7. Process maps showing the variation of (Y/σ_y) for different combinations of scanning speed and preheat temperature for LPBF of (a) Ti6Al4V, (b) IN718, (c) SS316 (d) AlSi10Mg alloy calculated using Eq. (29). Other process parameters are kept constant as: laser power = 250 W, laser spot diameter = 100 μm, layer thickness = 40 μm, hatch spacing = 100 μm, track length = 5 mm.

.

The small deviation between the numerically computed [56] and the corresponding analytically calculated residual stress is attributed to the variabilities in the estimated values of the melt pool depth (δ) and peak residual stress (Y) using the scaling relations. It is also noteworthy that the numerical model could consider the application of boundary conditions in a more compliant manner in comparison to the analytical model calculations presented here. Nevertheless, Fig. 8(b) shows that the proposed analytical model can fairly estimate the residual stress distributions for LPBF of a multilayer part with Ti6Al4V powder. Indeed, analytically calculated residual stress distributions through the build parts with a large number of layers and diverse LPBF conditions are required to examine further to check the efficiency and robustness of the proposed model.

4.2. LPBF of a 334-layer deposit of AlSi10Mg

The analytical model is further tested to calculate the residual stress distributions for the LPBF of a cube with 334 layers of AlSi10Mg alloy. Fig. 9(a) shows the cross-section of the part and baseplate and the locations where the residual stress is measured using the contour method [57]. Fig. 9(b) shows a comparison of the experimentally measured and the corresponding analytically computed residual stress distributions. The melt pool depth (δ) and the peak residual stress (Y) are estimated as 73 μm and 95 MPa using Eqs. (21) and (29), respectively. The evolution of the residual stress from the topmost layer through the underlying solidified layers and the baseplate is estimated recursively for the deposition of each new layer following Eqs. (14 and 15).

The analytically computed residual stress distributions in the part show a non-linear trend with tensile stress throughout the part. The stress decreases to 22 MPa at the bottom of the part followed by a sharp transition to a compressive stress of around 72 MPa through the part-baseplate interface as shown in Fig. 9(b). The stress distribution further varies linearly through the baseplate to a tensile stress of around 50 MPa at the bottom. The measured residual stress [57] remains tensile and also shows a non-linear trend through the part with a peak value of around 110 MPa at the top and 20 MPa at the bottom of the part. The measured residual stress becomes compressive at the top of the baseplate with a maximum value of around 70 MPa and varies nearly linearly to a tensile stress of 60 MPa at the bottom of the baseplate.

Fig. 9(b) shows a fair match between the experimentally measured [57] and the corresponding analytically calculated residual stress implying the practical usability of the proposed analytical model for LPBF. The analytical model is tested further for the calculations of residual stress distributions in a part with thousands of layers, which is difficult and nearly impossible to calculate numerically with commonly available computational hardware in a layer-by-layer manner.

4.3. LPBF of a 2000-layer deposit of IN718

The analytical model is further tested to calculate the residual stress distributions for LPBF of a relatively thin wall structure with 2000 layers

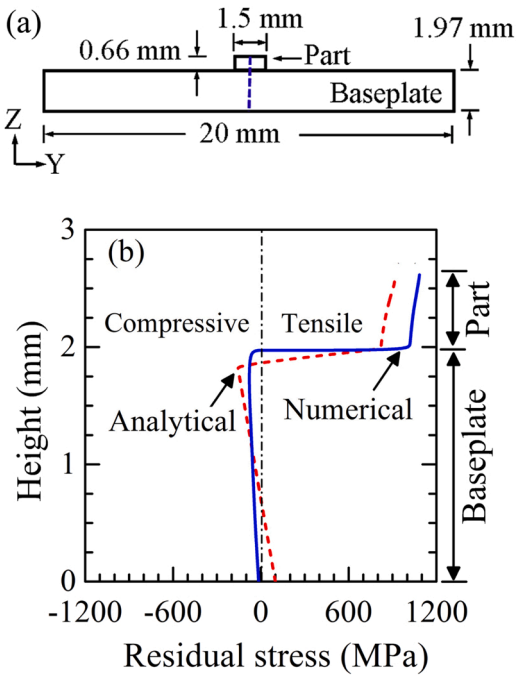

Fig. 8. (a) Schematic cross-section of a 22-layer deposit of Ti6Al4V powder on a baseplate [LPBF conditions: laser power = 270 W, scanning velocity = 1000 mm/s, laser spot diameter = 200 μm, layer thickness = 30 μm, hatch spacing = 100 μm]. (b) Comparison of numerically computed [56] and analytically calculated longitudinal residual stress distributions along the blue dashed line in (a).

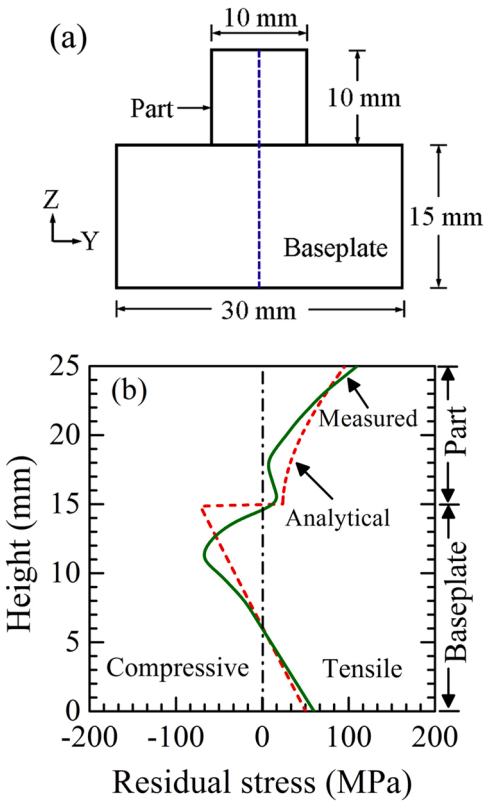

Fig. 9. (a) Schematic cross-section of a 334-layer deposit of AlSi10Mg powder on a baseplate [LPBF conditions: laser power = 370 W, scanning velocity = 1200 mm/s, laser spot diameter = 100 μm, layer thickness = 30 μm, hatch spacing = 170 μm]. (b) Comparison of experimentally measured [57] and analytically calculated longitudinal residual stress distributions along the blue dashed line in (a).

of IN718 powder. The total track length of the printed part was about 8000 m. Fig. 10(a) shows the cross-section of the part and baseplate along with the locations for the measurement of residual stress using neutron diffraction as reported in the literature [58]. Fig. 10(b) shows a comparison of the analytically computed residual stress distribution with the corresponding experimentally observed [58] and numerically computed [59] results. For the given LPBF conditions, the values of δ and Y are estimated respectively as 50 μm and 309 MPa using Eqs. (21) and (29). The residual stress follows a non-linear distribution through the part with tensile stress at the top and bottom and compressive stress at its mid-length. A sharp transition from tensile to compressive stress through the part-baseplate interface is also noted in Fig. 10(b). A large number of deposited layers and significant height of the part have resulted in a considerable redistribution of residual stress leading to a non-linear variation of stress in the part with compressive stress near to its mid-height.

Fig. 10(b) shows that the experimentally measured average stress at a location 2 mm below the top surface of the part is around 351 MPa [58] and the corresponding numerically computed stress is 330 MPa [59]. The analytically calculated stress at the same location is equal to around 280 MPa. The experimentally measured peak tensile and compressive stresses are around 57 MPa and 305 MPa at 2 mm above and 1.5 mm below the part-baseplate interface, respectively [58]. At these two locations, the numerical model provided tensile stress of around 188 MPa and compressive stress of around 285 MPa [59]. The corresponding stress values from the analytical model are equal to 62 MPa tensile and 243 MPa compressive, respectively. The analytically calculated stress through the depth of the baseplate shows a linear variation from compressive stress at the top to a tensile residual stress of around 277 MPa at the bottom. In comparison, the numerically computed [59] residual stress is around 60 MPa at the bottom of the part. No experimentally measured stress at the bottom of the baseplate is available in the reference [58].

The difference between the analytically and the numerically computed values [59] of the stress at the bottom of the baseplate is attributed to the edge effect in the analytical model. Similar values of residual stress distribution and transition of stress at the interface between the part and baseplate are also reported for directed energy deposition (DED) based additive manufacturing of IN718 [60]. A more generalized part is additionally considered to understand the effect of geometric complexity on the local stress distribution.

4.4. LPBF of a demonstrator part of IN625

Here we examine the use of the proposed analytical model to calculate residual stress distributions for LPBF of a realistic part with local variations in the cross-sections. Fig. 11(a) shows the considered part, which is a bridge structure with varying cross-sections from the bottom to the top and is produced by LPBF of around 625 layers with IN625 powder alloy [61]. The analytical model accounts for the change in layer-wise cross-section by considering a linear variation of Young's modulus of the alloy along the depth of the legs [62]. To start with the calculation of the residual stress distribution, the melt pool depth (δ) and the peak tensile residual stress (Y) are estimated as 69 μm and 432 MPa using Eqs. (21) and (29). A comparison of the analytically calculated residual stress distribution and, the corresponding experimentally measured [61] and the numerically computed results [63] is shown in Fig. 11(b). The measurement of residual stress in [61] was undertaken using the contour method and along the cross-section represented by the red lines in Fig. 11(a). The numerically computed stress was reported only for the part [63].

The distribution of residual stress in the part shows a non-linear trend with tensile stress at the top that gradually reduces and becomes

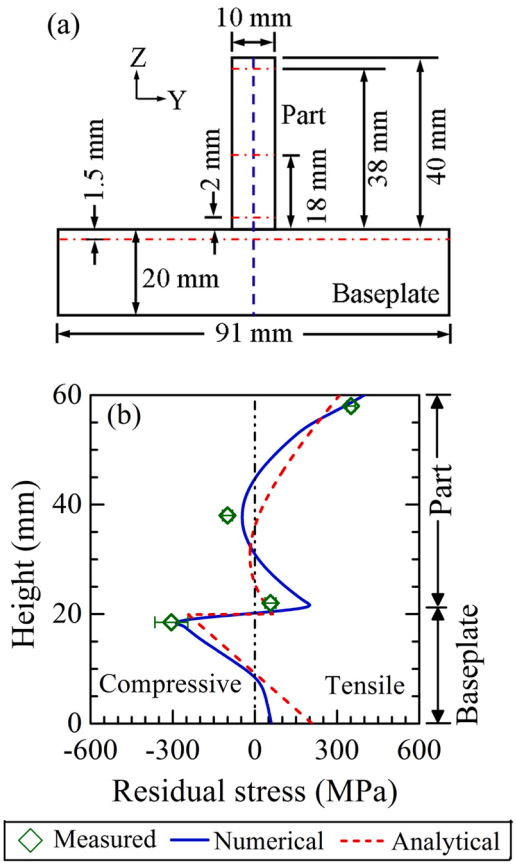

Fig. 10. (a) Schematic cross-section of a 2000-layer deposit of IN718 powder on a baseplate [LPBF conditions: laser power = 195 W, scanning velocity = 1200 mm/s, laser spot diameter = 100 μm, layer thickness = 20 μm, hatch spacing = 100 μm]. (b) Comparison of experimentally measured [58], numerically computed [59], and analytically calculated longitudinal residual stress distributions along the blue dashed line in (a).

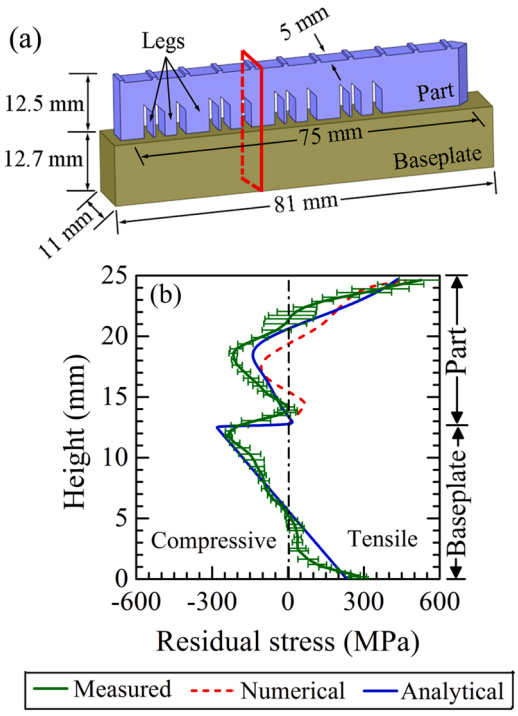

Fig. 11. (a) Schematic of a bridge structure, a 625-layer deposit of IN625 powder on a baseplate [LPBF conditions: laser power = 195 W, scanning velocity = 800 mm/s, laser spot diameter = 100 μm, layer thickness = 20 μm, hatch spacing = 100 μm]. (b) Comparison of experimentally measured [61], numerically computed [63], and analytically calculated longitudinal residual stress distributions along the section shown by the red outlined box in (a).

compressive through the legs followed by a sharp transition to a peak compressive stress at the part-baseplate interface and a gradual change to tensile stress towards the bottom of the baseplate. The reported values of the experimentally measured [61] and numerically computed [63] peak tensile stress at the top of the part are around 526 MPa and 460 MPa, respectively. At the mid-height of the part, a compressive residual stress of 142 MPa is predicted by the analytical model and the corresponding experimentally measured [61] and numerically computed [63] stresses are reported as 216 MPa and 107 MPa, respectively. Through the part-baseplate interface, the analytically calculated residual stress shows a peak compressive stress of 284 MPa, and the corresponding experimentally measured stress is 236 MPa [61]. At the bottom of the baseplate, the analytical computed and the corresponding experimentally measured [61] tensile stresses are 233 MPa and 276 MPa, respectively.

The discrepancy between the analytically computed residual stress and the corresponding measured [51] and numerically computed [53] results is attributed primarily to the limitation of the analytical model to account for appropriate boundary conditions and the layer-wise variations of the cross-section of the bridge structure. Fig. 12(a-d) shows a summary of the comparisons between the analytically calculated and the corresponding numerically computed [56] and experimentally measured [57,58,61] values of residual stress, which are presented in Sections (4.1–4.4) for LPBF of Ti6Al4V, AlSi10Mg, IN718, and IN625 parts. For each LPBF part, the residual stress near the bottom, middle and top are considered and designated as B, M, and T, respectively in Fig. 12(a-d). Overall, Fig. 12(a-d) shows a fair agreement between the reported values of numerically computed [56] and experimentally measured [57,58,61], and the corresponding analytically calculated values of residual stress with the accuracies of prediction between 70 % and 80 %. The difference is primarily attributed to the variabilities in the estimated values of the peak residual stress (Y) using the scaling relations and the limitation of the analytical model to account for appropriate boundary conditions.

5. Computational time

The aforementioned Sections (4.1–4.4) have shown the ability of the proposed analytical model for the calculation of residual stress distributions through the part and baseplate in LPBF of parts of simple and fairly complex geometry with commonly used alloy powders. The computational efficiency of the analytical model in comparison to the numerical process simulation models is presented in this section to examine the practical usability of the analytical models. Table 5 shows the model details, the hardware used, and the execution run times for the numerical simulations of residual stress, which are obtained from the literature for the validation of the analytically computed results in the aforementioned Sections (4.1–4.4). The numerical model [56], referred to in section-4.1, considered a finite element method based thermo-mechanical analysis for the LPBF of a 22-layer build of Ti6Al4V powder. The numerical model [59], which is referred to in section-4.3, undertook a finite element method based thermo-mechanical simulation for LPBF of a 2000-layer build of IN718 powder and considered one equivalent layer for every 20 layers to keep modeling calculations tractable. The finite element method-based thermo-mechanical simulation of the bridge structure [63], which is referred to in section-4.4, has also followed the lumping of multiple layers to reduce the computational demand.

A comparison of the simulation run times of these numerical models [56,59,63] with that for the analytical model is presented in Table 5.

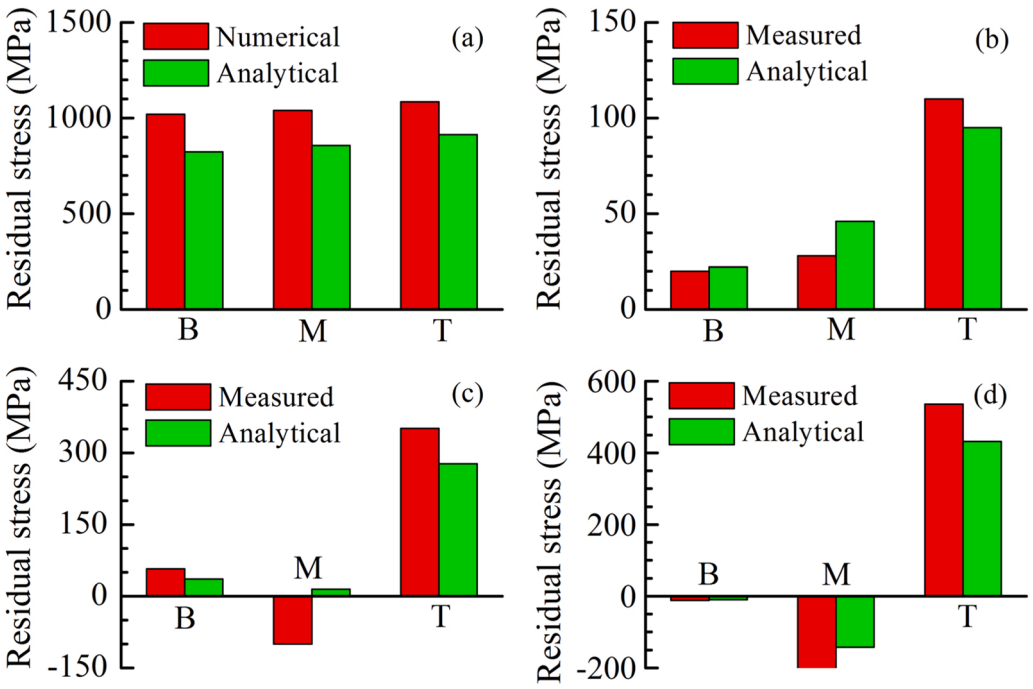

Fig. 12. Summary of comparison between residual stress predicted using the analytical model and corresponding numerically computed [56] or measured [57,58,61] stress presented in Sections 4.1–4.4 for (a) Ti6Al4V (b) AlSi10Mg (c) IN718 (d) IN625 alloy. The comparison is presented for the bottom (B), middle (M), and top (T) of the printed part.

Table 5
Execution times to compute residual stress distributions using FEM-based numerical models and proposed analytical model for LPBF of single and multiple layer depositions.

Sl. No.	Dimension (mm^3)	Simulation details				Single-core equivalent run time (hr)	
		Computed layers	Nodes	Elements	Hardware speed	Numerical	Analytical
1	20 × 1.5 × 0.66	22	844,071	784,900	2.8 GHz	~ 48[56]	0.002
2	40 × 10 × 40	200	427,850	401,380	2.7 GHz	~ 1632[a][59]	0.250
3	75 × 5 × 12.5	50	152,604	91,764	3.6 GHz	~ 6[63]	0.050

[a] Estimated based on simulation of a few computational layers.

The analytical model calculations are performed with an 11th generation core i5 notebook computer with 8 GB RAM and 4.2 GHz hardware speed. Overall, Table 5 shows that the analytical model could simulate a typical part scale volume of 1600 mm^3 with 2000 layers of deposition in less than 15 min. For all these three cases considered, the analytical model performed the calculations more than 10,000 times faster compared to the numerical models. Although the numerical models could undertake a coupled thermo-mechanical analysis, the consideration of the individual layers for a part scale geometry has remained intractable. Furthermore, numerical modeling with reduced order geometry also requires huge execution times, which are impractical for routine calculations with inexpensive computer hardware [49]. In contrast, the analytical model can undertake layer-by-layer deposition of powder alloys as well as consider layer-wise variations of the geometric cross-sections and has shown a fairly competitive accuracy in calculated results of residual stress distributions.

The aforementioned sections have shown the utility of the proposed analytical model in terms of the accuracy of predicted residual stress and its computational efficiency. The analytical model follows the mechanistic principles of the equilibrium of forces and moments and the computed residual stress distributions from the model have exhibited its strength to be used as a practical tool for the estimation of residual stress distribution for LPBF of small to large parts. Although the proposed analytical model cannot provide the transverse and normal component of residual stress as well as the three-dimensional distribution of stress, it can offer a fairly effective estimation of the longitudinal residual stress in the part away from the boundary. The analytical model is easy to implement and does not require any high-performance computing resources which are essential for numerical models.

6. Summary and conclusions

A model for the analytical calculation of longitudinal residual stress distribution for LPBF in parts scale is presented and tested against independent numerical calculations and experimental data. The solution involves the calculation of the melt pool depth and the peak tensile residual stress for the deposition of individual layers nearly 10,000 times faster than the available numerical models. The analytically calculated residual stress distributions were validated with independent experimental data and numerically computed results for different geometries during LPBF of a wide range of conditions. The following are the main conclusions.

- It is shown that lower laser power, faster scanning speeds and higher preheat temperatures are desirable to reduce the peak residual stress. An increase in scanning speed and preheat temperature has the steepest reduction in peak tensile residual stress.
- Among the five alloy powders considered here, LPBF of Ti6Al4V and AlSi10Mg showed the maximum and minimum residual stress build-up, respectively for the same laser power and scanning speed. The

lower thermal diffusivity of Ti6Al4V leads to a higher temperature gradient and thermal strains.

- The computed results show a significant contribution of the part dimensions towards the distribution of residual stress in parts. For a relatively thin part with low height, the stress in the part is tensile. However, as the part height increases, the residual stress near the mid-height of the part tends to become compressive and remains tensile at the top and bottom.
- The proposed analytical model can compute the evolution of residual stress in several thousands of deposited layers many times faster than the numerical models. For example, the residual stress distribution for LPBF of a build volume of 1600 mm^3 can be analyzed in 15 min using a core i5 notebook computer with 8 GB RAM.

CRediT authorship contribution statement

Kajal Khan : Writing - original draft, Validation, Methodology, Formal Analysis, Data curation, Conceptualization. **L Srinivasa Mohan :** Writing - review. **Amitava De :** Writing - original draft, review & editing, Validation, Supervision, Methodology, Investigation, Conceptualization. **Tarasankar DebRoy :** Writing - review & editing. Visualization. Supervision. Methodology.

Declaration of Competing Interest

The authors declare that they have no known competing financial interests or personal relationships that could have appeared to influence the work reported in this paper.

Data availability

Data will be made available on request.

References

[1] S.L. Sing, W.Y. Yeong, Laser powder bed fusion for metal additive manufacturing: perspectives on recent developments, Virtual Phys. Prototyp. 15 (2020) 359–370.

[2] T. DebRoy, H.L. Wei, J.S. Zuback, T. Mukherjee, J.W. Elmer, J.O. Milewski, A. M. Beese, A. Wilson-Heid, A. De, W. Zhang, Additive manufacturing of metallic components – process, structure and properties, Prog. Mater. Sci. 92 (2018) 112–224.

[3] W.J. Lai, A. Ojha, Z. Li, C.E. Pinto, X. Su, Effect of residual stress on fatigue strength of 316L stainless steel produced by laser powder bed fusion process, Prog. Addit. Manuf. 6 (2021) 375–383, https://doi.org/10.1007/s40964-021-00164-8.

[4] K. Khan, G. Mohr, K. Hilgenberg, A. De, Probing a novel heat source model and adaptive remeshing technique to simulate laser powder bed fusion with experimental validation, Comput. Mater. Sci. 181 (2020), 109752.

[5] E.R. Denlinger, J. Irwin, P. Michaleris, Thermomechanical modeling of additive manufacturing large parts, ASME J. Manuf. Sci. Eng. 136 (6) (2014), 061007, https://doi.org/10.1115/1.4028669.

[6] K. Khan, A. De, Modelling of selective laser melting process with adaptive remeshing, Sci. Technol. Weld. Join. 24 (5) (2019) 391–400, https://doi.org/10.1080/13621718.2019.1575057.

[7] N. Patil, R. Ganeriwala, J.M. Solberg, N.E. Hodge, R.M. Ferencz, Benchmark multi-layer simulations for residual stresses and deformation in small additively manufactured metal parts, Addit. Manuf. 45 (2021), 102015.

[8] C.H. Fu, Y. Guo, 3-dimensional finite element modeling of selective laser melting Ti-6Al-4V alloy, In: Proceedings of the 25th SFF Symposium, Austin, TX, USA, 2014, pp. 1129–1144.

[9] R. Tangestani, T. Sabiston, A. Chakraborty, L. Yuan, N. Krutz, E. Martin, An efficient track-scale model for laser powder bed fusion additive manufacturing: part 2 – mechanical model, Front. Mater. 8 (2021), https://doi.org/10.3389/fmats.2021.759669.

[10] R. Ganeriwala, M. Strantza, W. King, B. Clausen, T.Q. Phan, L.E. Levine, D. W. Brown, N. Hodge, Evaluation of a thermomechanical model for prediction of residual stress during laser powder bed fusion of Ti-6Al-4V, Addit. Manuf. 27 (2019) 489–502.

[11] F. Hajializadeh, A. Ince, Finite element-based numerical modeling framework for additive manufacturing process, Mater. Des. Process. Commun. 1 (1) (2019), https://doi.org/10.1002/mdp2.28.

[12] M. Shiomi, K. Osakada, K. Nakamura, T. Yamashita, F. Abe, Residual stress within metallic model made by selective laser melting process, CIRP Ann. -Manuf. Technol. 53 (1) (2004) 195–198.

[13] P. Mercelis, J.P. Kruth, Residual stresses in selective laser sintering and selective laser melting, Rapid Prototyp. J. 12 (5) (2006) 254–265.

[14] D. Boruah, X. Zhang, M. Doré, An analytical method for predicting residual stress distribution in selective laser melted/sintered alloys, Mater. Res. 6 (2018) 283–288.

[15] V. Chahal, R.M. Taylor, Model development for residual stress consideration in design for laser metal 3DPrinting of maraging Steel 300. In: Proceedings of the 29th SFF Symposium, Austin, TX, USA, 2018, p. 623–634.

[16] E. Mirkoohi, H.C. Tran, Y.L. Lo, Y.C. Chang, H.Y. Lin, S.Y. Liang, Mechanics modeling of residual stress considering effect of preheating in laser powder bed fusion, J. Manuf. Mater. Process 5 (46) (2021), https://doi.org/10.3390/jmmp5020046.

[17] J. Ning, M. Praniewicz, W. Wang, J.R. Dobbs, S.Y. Liang, Analytical modeling of part distortion in metal additive manufacturing, Int. J. Adv. Manuf. Technol. 107 (2020) 49–57, https://doi.org/10.1007/s00170-020-05065-8.

[18] J. Ning, D.E. Sievers, H. Garmestani, S.Y. Liang, Analytical modeling of in-process temperature in powder bed additive manufacturing considering laser power absorption, latent heat, scanning strategy, and powder packing, Materials 12 (5) (2019) 808, https://doi.org/10.3390/ma12050808.

[19] J. Ning, D.E. Sievers, H. Garmestani, S.Y. Liang, Analytical modeling of part porosity in metal additive manufacturing, Int. J. Mech. Sci. 172 (2020), 105428.

[20] Y. Liu, Y. Yang, D. Wang, A study on the residual stress during selective laser melting (SLM) of metallic powder, Int. J. Adv. Manuf. Technol. 87 (2016) 647–656.

[21] B. Cheng, S. Shrestha, K. Chou, Stress and deformation evaluations of scanning strategy effect in selective laser melting, Addit. Manuf. 12 (2016) 240–251.

[22] S. Timoshenko. Strength of Materials - Part 1, second ed., D Van Nostrand Co Inc,, London (UK), 1940.

[23] S. Liu, Y.C. Shin, Additive manufacturing of Ti6Al4V alloy: a review, Mater. Des. 164 (2019), 107552.

[24] C. Li, J.F. Liu, Y.B. Guo, Prediction of residual stress and part distortion in selective laser melting, Procedia CIRP 45 (2016) 171–174.

[25] J. Metelkova, Y. Kinds, K. Kempen, C. de Formanoir, A. Witvrouw, B. Van Hooreweder, On the influence of laser defocusing in selective laser melting of 316L, Addit. Manuf. 23 (2018) 161–169, https://doi.org/10.1016/j.addma.2018.08.006.

[26] U.S. Bertoli, A.J. Wolfer, M.J. Matthews, J.R. Delplanque, J.M. Schoenung, On the limitations of volumetric energy density as a design parameter for selective melting, Mater. Des. 113 (2017) 331–340.

[27] B. Vrancken, R. Wauthle, J.P. Kruth, J.V. Humbeeck, Study of the Influence of Material Properties on Residual Stress in Selective Laser Melting, In: Proceedings of the SFF Symposium, Austin, TX, USA, 2013, pp. 393–407.

[28] K.C. Mills, Recommended Values of Thermo-Physical Properties for Selected Commercial Alloys, Woodhead Publishing,, Cambridge, 2002.

[29] EOS GmbH - Electro Optical Systems. EOS Nickel Alloy IN625; Material Data Sheet; EOS GmbH: Krailling, Germany, 2010.

[30] R. Cunningham, C. Zhao, N. Parab, C. Kantzos, J. Pauza, K. Fezzaa, T. Sun, A. D. Rollett, Keyhole threshold and morphology in laser melting revealed by ultrahigh-speed x-ray imaging, Science 363 (6429) (2019) 849–852.

[31] E. Soylemez, Modeling the melt pool of the laser sintered Ti6Al4V layers with Goldak's double-ellipsoidal heat source, In: Proceedings of the 29th SFF Symposium, Austin, TX, USA, 2018, pp. 13–15.

[32] M. Balbaa, S. Mekhiel, M. Elbestwai, J. Mclsaac, On selective laser melting of Inconel 718: densification, surface roughness, and residual stresses, Mater. Des. 193 (2020), 108818.

[33] M. Sadowski, L. Ladani, W. Brindley, J. Romano, Optimizing quality of additively manufactured Inconel 718 using powder bed laser melting process, Addit. Manuf. 11 (Suppl. C) (2016) 60–70, https://doi.org/10.1016/j.addma.2016.03.006.

[34] P. Kumar, J. Farah, J. Akram, C. Teng, J. Ginn, M. Misra, Influence of laser processing parameters on porosity in Inconel 718 during additive manufacturing, Int. J. Adv. Manuf. Technol. 103 (2019) 1497–1507.

[35] Q. Chen, Y. Zhao, S. Strayer, Y. Zhao, K. Aoyagi, Y. Koizumi, A. Chiba, W. Xiong, A. C. To, Elucidating the effect of preheating temperature on melt pool morphology variation in Inconel 718 laser powder bed fusion via simulation and experiment, Addit. Manuf. 37 (2021), 101642.

[36] L.E. Criales, Y.M. Arısoy, B. Lane, S. Moylan, A. Donmez, T. Özel, Laser powder bed fusion of nickel alloy 625: experimental investigations of effects of process parameters on melt pool size and shape with spatter analysis, Int. J. Mach. Tool. Manuf. 121 (2017) 22–36.

[37] J.S. Dilip, M.A. Anam, D. Pal, B. Stucker, A short study on the fabrication of single track deposits in SLM and characterization, In: Proceedings of the 27th SFF Symposium, Austin, TX, USA, 2016, pp. 1644–1659.

[38] C. Kamath, B. El-dasher, G.F. Gallegos, W.E. King, A. Sisto, Density of additively-manufactured, 316L SS parts using laser powder-bed fusion at powers up to 400 W, Int. J. Adv. Manuf. Technol. 74 (2014) 65–78.

[39] K. Kempen, L. Thijs, E. Yasa, M. Badrossamay and W. Verheecke, J. Kruth, Process optimization and microstructural analysis for selective laser melting of AlSi10Mg, In: Proceedings of the SFF Symposium, Austin, TX, USA, 2011, pp. 484–495.

[40] H. Hyer, Le Zhou, S. Park, G. Gottsfritz, G. Benson, B. Tolentino, B. McWilliams, K. Cho, Y. Sohn, Understanding the laser powder bed fusion of AlSi10Mg alloy, Metallogr. Microstruct. Anal. 9 (2020) 484–502, https://doi.org/10.1007/s13632-020-00659-w.

[41] T. Mishurova, K. Artzt, J. Haubrich, G. Requena, G. Bruno, New aspects about the search for the most relevant parameters optimizing SLM materials, Addit. Manuf. 25 (2019) 325–334.

[42] B. Vrancken, S. Buls, J.P. Kruth, J.V. Humbeeck, Influence of preheating and oxygen content on selective laser melting of Ti6Al4V, In: Proceedings of the 16th RAPDASA Conference, Pretoria, South Africa, 2015.

[43] M.A. Balbaa, M.A. Elbestawi, J. McIsaac, An experimental investigation of surface integrity in selective laser melting of Inconel 625, Int. J. Adv. Manuf. Technol. 104 (2019) 3511–3529.
[44] M. Yakout, M.A. Elbestawi, S.C. Veldhuis, Density and mechanical properties in selective laser melting of Invar 36 and stainless steel 316L, J. Mater. Process. Technol. 266 (2019) 397–420.
[45] P. Bian, J. Shi, Y. Liu, Y. Xie, Influence of laser power and scanning strategy on residual stress distribution in additively manufactured 316L steel, Opt. Laser Technol. 132 (2020), 106477.
[46] T. Simson, A. Emmel, A. Dwars, J. Böhm, Residual stress measurements on AISI 316L samples manufactured by selective laser melting, Addit. Manuf. 17 (2017) 183–189.
[47] L. Wang, X. Jiang, Y. Zhu, Z. Ding, X. Zhu, J. Sun, B. Yan, Investigation of performance and residual stress generation of AlSi10Mg processed by selective laser melting, Adv. Mater. Sci. Eng. 2018 (2018), 7814039, https://doi.org/10.1155/2018/7814039.
[48] Y. Chen, H. Sun, Z. Li, Y. Wu, Y. Xiao, Z. Chen, S. Zhong, H. Wang, Strategy of residual stress determination on selective laser melted Al alloy using XRD, Materials 13 (2) (2020) 451.
[49] S. Bagherifard, N. Beretta, S. Monti, M. Riccio, M. Bandini, M. Guagliano, On the fatigue strength enhancement of additive manufactured AlSi10Mg parts by mechanical and thermal post-processing, Mater. Des. 145 (2018) 28–41.
[50] P. Zagade, B.P. Gautham, A. De, T. DebRoy, Analytical estimation of fusion zone dimensions and cooling rates in part scale laser powder bed fusion, Addit. Manuf. 46 (2021), 102222.
[51] T. Mukherjee, J. Zuback, A. De, T. DebRoy, Printability of alloys for additive manufacturing, Sci. Rep. 6 (2016) 19717.
[52] Q. Wu, T. Mukherjee, A. De, T. DebRoy, Residual stresses in wire-arc additive manufacturing–Hierarchy of influential variables, Addit. Manuf. 35 (2020), 101355.
[53] B. Vrancken, Study of Residual Stresses in Selective Laser Melting [Thesis], KU Leuven Faculty of Engineering Science,, Leuven (Belgium), 2016.
[54] M. Yakout, M. Elbestawi, S. Veldhuis, Influence of thermal properties on residual stresses in SLM of aerospace alloys, Rapid Prototype J. 26 (1) (2020) 213–222.
[55] T. Mukherjee, V. Manvatkar, A. De, T. DebRoy, Dimensionless numbers in additive manufacturing, J. Appl. Phys. 121 (2017), 064904.
[56] X. Zhao, A. Iyer, P. Promoppatum, S.C. Yao, Numerical modeling of the thermal behavior and residual stress in the direct metal laser sintering process of titanium alloy products, Addit. Manuf. 14 (2017) 126–136.
[57] E.S. Statnik, F. Uzun, S.A. Lipovskikh, Y.V. Kan, S.I. Eleonsky, V.S. Pisarev, P. A. Somov, A.I. Salimon, Y.V. Malakhova, A.G. Seferyan, D.K. Ryabov, A. M. Korsunsky, Comparative multi-modal, multi-scale residual stress evaluation in SLM 3D-printed Al-Si-Mg alloy (RS-300) parts, Metals 11 (12) (2021) 2064, https://doi.org/10.3390/met11122064.
[58] F. Bayerlein, F. Bodensteiner, C. Zeller, M. Hofmann, M.F. Zaeh, Transient development of residual stresses in laser beam melting – a neutron diffraction study, Addit. Manuf. 24 (2018) 587–594.
[59] P. Promoppatum, V. Uthaisangsuk, Part scale estimation of residual stress development in laser powder bed fusion additive manufacturing of Inconel 718, Finite Elem. Anal. Des. 189 (2021), 103528.
[60] T. Mukherjee, W. Zhang, T. DebRoy, An improved prediction of residual stresses and distortion in additive manufacturing, Comput. Mater. Sci. 126 (2017) 360–372.
[61] T.Q. Phan, M. Strantza, M.R. Hill, T.H. Gnaeupel-Herold, J.C. Heigel, C.R. D'Elia, A.T. DeWald, B. Clausen, D.C. Pagan, P. Ko, D.W. Brown, L.E. Levine, Elastic residual strain and stress measurements and corresponding part defections of 3D additive manufacturing builds of IN625 AM-bench artifacts using neutron difraction, synchrotron X-ray difraction, and contour method, Integr. Mater. Manuf. Innov. 8 (2019) 318–334.
[62] A.K. Kaw, Mechanics of Composite Materials, Taylor & Francis,, United Kingdom, 2005.
[63] A. Olleak, Z. Xi, A study of modeling assumptions and adaptive remeshing for thermomechanical finite element modeling of the LPBF process, Int. J. Adv. Manuf. Technol. 115 (2021) 3599–3615, https://doi.org/10.1007/s00170-021-07362-2.